FISEVIER

Contents lists available at ScienceDirect

Mechanical Systems and Signal Processing

journal homepage: www.elsevier.com/locate/ymssp



Impact force sensing with magnetostrictive Fe-Ga alloys



Liang Shu^{a,*}, Jiabin Yang^b, Bo Li^b, Zhangxian Deng^c, Marcelo J. Dapino^d

- ^a The Key Laboratory of Low-Voltage Apparatus Intellectual Technology of Zhejiang, Wenzhou University, Wenzhou 325000, Zhejiang Province, China
- ^b College of Logistics Engineering, Wuhan University of Technology, 430063 Wuhan, China
- ^c Department of Mechanical and Biomedical Engineering, Boise State University, Boise, ID 83725, USA
- d NSF IUCRC on Smart Vehicle Concepts, Department of Mechanical and Aerospace Engineering, The Ohio State University, Columbus, OH 43210, USA

ARTICLE INFO

Article history: Received 31 January 2019 Received in revised form 15 July 2019 Accepted 4 October 2019 Available online 31 October 2019

Keywords: Magnetostrictive Fe-Ga alloy Impact force sensing Orthogonal design

ABSTRACT

Fe-Ga alloys (Galfenol) are structural magnetostrictive materials which undergo magnetization changes when subjected to mechanical stress. They are machinable and can withstand large normal or shear stresses. Based on these unique features, this study develops an impact force sensor which consists of an electromagnet, magnetic circuit, cantilevered Fe-Ga alloy beam, and pickup coil. The external impact force generates a stress-induced flux density that is measured by the pickup coil. An axial impact sensor based on a Fe-Ga rod is constructed for comparison. Analytical modeling shows that the sensitivity of the cantilevered beam configuration is 11.27 times higher than that of the rod configuration. Three different geometries, including a rectangular beam, a uniform I beam, and a tapered I beam, are designed and compared. Analytical modeling shows that the tapered I beam exhibits maximum sensitivity. The optimized tapered I beam-based sensor is constructed experimentally and benchmarked against a similar sensor based on a Fe-Ga rod. A nonlinear Levenberg-Marquardt fitting method is used to correlate the input impact force with the resulting flux density variation. Experimental results show that the measurement error is within 5.8% for various impact amplitudes.

© 2019 Elsevier Ltd. All rights reserved.

1. Introduction

Precise measurement of impact force is the basis for vibration control strategies mitigating the negative effects of impact excitations [1]. However, the development of impact force sensors is currently constrained by two challenges: (1) the sensor needs to react fast enough to measure the short duration of impact excitations; (2) the sensing element needs to withstand the high energy density associated with the impact force. The impact force has been measured by a resistance strain gauge [2,3]. Due to the adhesive applied between the gauge and the target surface, the sensing accuracy is affected by the bonding process [4].

Smart materials and structures including piezoelectric materials [5–14], Fiber Bragg Grating [15–18], and magnetostrictive materials [19–26] have been utilized in force sensing. Piezoelectric materials, such as quartz, are able to convert mechanical impact into electrical charges [6]. Wang et al. [7] developed a quartz crystal resonator (QCR) and measured the stress-induced charges indirectly from the frequency variation of the QCR. A multi-axis force sensor [8] was also developed by incorporating four groups of quartz crystals. Piezoelectric impact sensors exhibit high linearity, negligible hysteresis, and fast response. However, they are capacitive sources with high electrical impedance and the stress-induced charge may

E-mail address: shuliangalbert@163.com (L. Shu).

^{*} Corresponding author.

leak rapidly over time [7]. Thus, complicated electrical circuits and signal analyzers are typically required to address these issues. Compared to brittle piezoelectric crystals or ceramics [9], piezoelectric polymers, such as PVDF films, exhibit moderate sensitivities while maintaining high flexibility and corrosion resistance [10–11]. PVDF-based single-axis and multi-axis impact force sensors have been developed by Kotian et al. [12] and Hwang and Hwang [13], respectively. However, stress applied along the thickness (poled) direction may damage the sensor system [12–13]. Similar to strain gauges, PVDF films are usually bonded to the main structure via adhesives. Hence, the performance of PVDF is sensitive to the bonding process [14].

Fiber Bragg Grating that reflects particular wavelengths of light can be implemented in impact detection [15–18]. FBG sensors are compact, corrosion resistant, and immune to electromagnetic interference. However, the FBG sensor is fragile and a high-frequency interrogator is necessary for signal post-processing. Moreover, FBG sensors are usually bonded to the target structures, thus, the bonding process greatly affects the sensing accuracy [17–18].

Magnetostrictive materials undergo magnetization changes when exposed to external stress [20]. Terbium-iron-dysprosium alloys (Terfenol-D) [21] and Fe-Ga alloys [22], that exhibit significant magnetostriction, have been implemented in force sensor designs. Terfenol-D is brittle in tension (about 28 MPa), so Terfenol-D devices are designed such that the active element always operates in pure compression or within complicated protection mechanisms [23]. Piezoelectric ceramics have a similar fragile nature and their tensile strength is 44.5 MPa [24]. Excessive bending or high longitudinal stresses may lead to material failure [25]. Fe-Ga alloy is a metallic solid with the property to withstand tension stresses up to 500 MPa. With different composition of iron and gallium, Fe-Ga can be safely placed in the load path without external protection, leading to a much simpler device structure. Fe-Ga alloys can be machined, welded, extruded, and deposited into complex geometries [26], and have adequate thermal stability as well as a relatively high Curie temperature of over 500 °C. With different concentration of gallium, the Curie temperature of Fe-Ga can be as high as 700 °C [27]. In contrast, the Curie points of Terfenol-D and piezoelectric ceramics are 380 °C [28] and 250 °C [24], respectively. Due to these unique properties, Fe-Ga alloys have been investigated in impact force detection. Most of the force sensors are based on magnetostrictive rods and exhibit relatively low sensitivities [29]. The research of existing magnetostrictive force sensors is constrained in the static or quasi-static regimes. Scheidler et al. [30] first presented dynamic flux density versus stress measurement up to 1 kHz using a rod configuration. However, the literature on high sensitivity impact detection utilizing magnetostrictive materials is limited.

This study develops, optimizes, and characterizes impact force sensors based on polycrystalline, $\langle 1\ 0\ 0 \rangle$ -oriented, Fe-Ga alloys (18.4% Ga). The impact force is directly applied on the Fe-Ga component. Three types of Fe-Ga beam configurations are investigated. The performance of the beam configurations is benchmarked against the rod configuration. The sensing principle is described in Section 2. Kinetic models calculating the average strain are developed analytically for the rod and beam configurations, respectively, in Sections 3 and 4. In Section 4, an orthogonal design method is developed to optimize the dimensions of the tapered I beam and the uniform I beam. Experimental results of the rod and the optimized tapered I beam are presented and analyzed in Section 6.

2. Sensing principle

The Fe-Ga alloy materials undergo magnetization changes when exposed to external stress. The induced flux density can be approximated by [31]

$$\Delta B = d \cdot \Delta T + \mu^H \cdot \Delta H,\tag{1}$$

where d is the piezomagnetic coefficient, μ^H is the magnetic permeability, ΔH is the magnetic field increment, ΔT is the stress increment, and ΔB is the corresponding increment in flux density. When the bias field is properly designed, the sensor is working in the linear region and the increment of flux density can be described with a linear piezomagnetic law [32],

$$\Delta B = d \cdot \Delta T. \tag{2}$$

Following Faraday's law, ΔB induces an electrical voltage V(t) on a pickup coil wrapped around the Fe-Ga element

$$V(t) = -NA \cdot \frac{\partial B}{\partial t} = -NA \cdot d \cdot \frac{\partial T}{\partial t} = -NA \cdot d \cdot E \cdot \frac{\partial \varepsilon(F)}{\partial t}, \tag{3}$$

where N is the total number of turns, A is the coil's cross section, E is the Young's modulus, and E is the strain, described as a function of external force E. Thus, the flux density has the form

$$B = \int_0^{\Delta t} \frac{V(t)}{-NA} dt = \int_0^{\Delta t} d \cdot E \cdot \frac{\partial \varepsilon}{\partial t} dt = d \cdot T(F). \tag{4}$$

The sensitivity of a Fe-Ga alloy force sensor is defined as the ratio of flux density to force. In the linear region, values of *d* can be approximated as constant. The sensing sensitivity is thus proportional to the stress experienced by the Fe-Ga element.

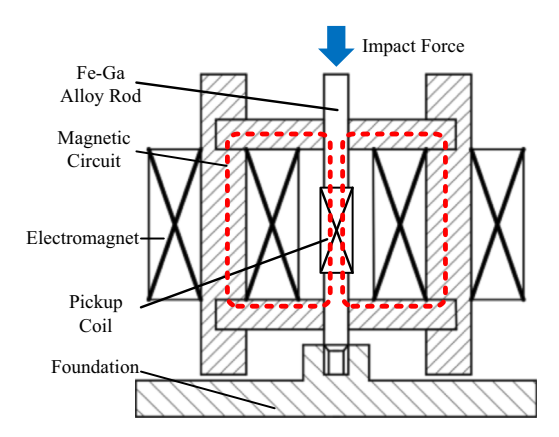


Fig. 1. The schematic of the impact force sensor based on a Fe-Ga rod.

3. Fe-Ga rod configuration

The rod configuration is firstly investigated and the configuration is presented in Fig. 1. A pair of electromagnets driven by DC currents generate a bias magnetic field through the Fe-Ga rod. Due to the magneto-mechanical coupling in Fe-Ga, the impact force applied on the free end introduces flux density variation and thus voltage on the pickup coil. Following (4), the magnetic flux density *B* can be correlated with the impact force if the strain-force relationship is known.

Assuming the impact-induced structural vibration is longitudinal, the free body diagram of a differential beam element of the Fe-Ga rod is shown in Fig. 2. The strain is expressed as $\varepsilon = \partial u/\partial x$, and the internal force on the cross section is expressed as $P = ES\varepsilon = ES \cdot \partial u/\partial x$. The following governing equation can be obtained from d'Alembert's Principle,

$$\frac{\partial^2 u}{\partial t^2} + \frac{c}{\rho S} \frac{\partial^2 u}{\partial t \partial x} = \frac{E}{\rho} \frac{\partial^2 u}{\partial x^2} + \frac{1}{\rho S} f(x, t). \tag{5}$$

where c is the internal damping coefficient. The damping consists of internal damping (distributed damping on the cross-section) and external damping (damping produced by an external medium on the body). For longitudinal vibrations, the effect of internal damping is far greater than the effect of external damping. Therefore, only internal damping is included in this study.

The mode-summation method is used to solve (5). It is assumed that

$$u(x,t) = \sum_{i=1}^{\infty} \varphi_i(x)g_i(t), \tag{6}$$

where $\varphi_i(x)$ is normal mode, and $g_i(t)$ is a generalized coordinate. Substitute (6) into (5) and assume the damping term to be a Rayleigh damping,

$$M_i\ddot{g}_i(t) + C_i\dot{g}_i(t) + K_ig_i(t) = Q_i(t), \tag{7}$$

where the *i*th generalized mass is $M_i = \int_0^{L_R} \rho S \varphi_i(x) \varphi_i(x) dx = 1$, the *i*th generalized stiffness is $K_i = \int_0^{L_R} E S \varphi_i'(x)^2 dx$, the *i*th generalized damping is $C_i = 2\zeta_i \omega_i M_i$, where ζ_i denotes the damping ratio, ω_i is the *i*th natural frequency, and the *i*th generalized force is $Q_i(t) = \int_0^{L_R} \varphi_i(x) f(x,t) dx$. In this study, the only body force is the impact force F(t), so $Q_i(t) = \int_0^{L_R} F(t) \varphi_i(x) \delta(x - L_R) dx = \varphi_i(L_R) F(t)$.

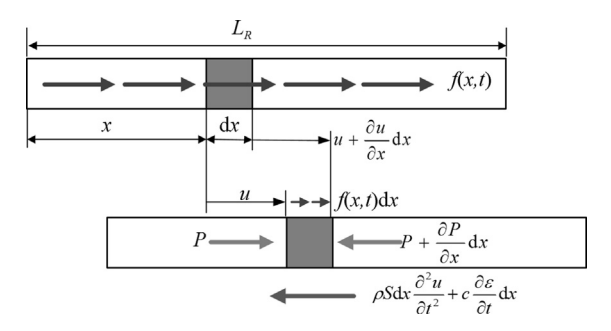


Fig. 2. Free body diagram of a differential beam element of the Fe-Ga rod, where f(x,t) is applied external force per unit length, L_R is length of the rod, S is cross section of the rod, ρ is density, u is the longitudinal displacement of the cross section of the rod, c is strain damping coefficient, ε is the strain, and P is internal force on the cross section.

The displacement u(x, t) is solved using Duhamel's integral as

$$u(x,t) = \sum_{i=1}^{\infty} \varphi_i(x) \cdot \frac{\varphi_i(L_R)}{M_i \omega_{di}} \cdot G_i(t)$$

$$G_i(t) = \int_0^t F(\tau) e^{-\zeta_i \omega_i(t-\tau)} \sin \omega_{di}(t-\tau) d\tau,$$
(8)

where $\omega_{di} = \omega_i \sqrt{1 - \zeta_i^2}$ is the *i*th damped vibration frequency. The strain is

$$\varepsilon(x,t) = \frac{\partial u(x,t)}{\partial x} \tag{9}$$

The modes and natural frequencies of the fixed-free rod are [33]

$$\begin{aligned} \omega_{i} &= \frac{(2i-1)\pi}{2L} \sqrt{\frac{E}{\rho}} \\ \varphi_{i}(x) &= D_{i} \phi_{i}(x), \quad \phi_{i}(x) = \sin \frac{\omega_{i}}{\sqrt{\frac{E}{\rho}}} x, \end{aligned} \tag{10}$$

where the coefficient D_i is obtained by solving

$$D_i = \sqrt{\frac{1}{\rho S} \frac{1}{\int_0^{L_R} \phi_i(x) \phi_i(x) dx}}.$$
 (11)

Insertion of (10) into (9) gives

$$\varepsilon(x,t) = \sum_{i=1}^{\infty} D_i^2 \frac{\partial \phi_i(x)}{\partial x} \cdot \frac{\phi_i(L_R)}{\omega_{di}} \cdot G_i(t). \tag{12}$$

4. Beam configuration

Beam configurations have been widely adopted in the existing literature [34,35]. If Fe-Ga alloy is operated in bending, it could experience higher strain and thus can potentially provide a higher sensitivity. Fig. 3 shows a schematic of the impact force sensor based on a Fe-Ga beam. Similar to the rod configuration, an electromagnet excited by a DC current generates a bias magnetic field through the Fe-Ga beam. The voltage on the pickup coil can be correlated with the impact force applied on the free end of the beam.

For a single layer, monolithic Fe-Ga beam, half of the beam is in tension and the other half is in compression. Hence, the stress-induced flux density variation in each half cancels out and generates negligible voltage on the pickup coil when the Fe-Ga beam is biased at the center of its burst region. To avoid this effect, the magnetic field is selected to saturate the Fe-Ga alloy. When an impact force is applied, the half that experiences tensile stress remains in saturation, while the other half provides significant flux density variation in compression. As a result, a flux density variation reflecting the impact force can be introduced, even though the sensitivity is lower than it is for the unimorph beam configurations.

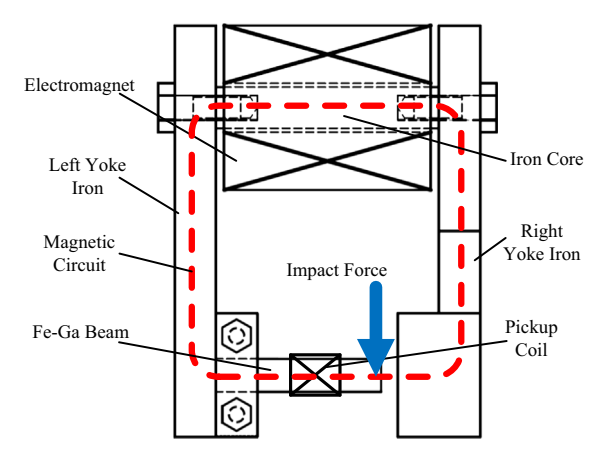


Fig. 3. Schematic of the impact force sensor based on a Fe-Ga beam.

4.1. Kinetic model for a rectangular beam configuration

The beam configuration based on a rectangular beam is first investigated through a kinetic model. Fig. 4 shows the free body diagram of a differential beam element of the Fe-Ga beam.

External and internal damping are both included in the model framework. The external damping force is assumed to be proportional to the vibration speed. The internal damping force is related to the strain rate of the material. The moment introduced by the internal damping is

$$M_D(x) = -c_s I(x) \frac{\partial^3 y(x,t)}{\partial x^2 \partial t},\tag{13}$$

where I(x) denotes the area moment of inertia, c_s denotes the strain damping coefficient, and y(x, t) denotes the deflection of the beam.

The bending moment M consists of $M_D(x)$ and the moment introduced by external damping. The governing equation for the beam is

$$\rho S \frac{\partial^2 y}{\partial t^2} + c \frac{\partial y}{\partial t} + \frac{\partial^2}{\partial x^2} \left(c_s I \frac{\partial^3 y}{\partial x^2 \partial t} + E I \frac{\partial^2 y}{\partial x^2} \right) = f(x, t) - \frac{\partial (x, t)}{\partial x}. \tag{14}$$

Following the same method introduced in Section 3, (14) can be written as

$$M_i\ddot{g}_i(t) + C_i\dot{g}_i(t) + K_ig_i(t) = Q_i(t),$$
 (15)

where $M_i = \int_0^{L_B} \rho S \varphi_i^2(x) dx$ is the ith normalized mass, L_B is the length of the beam, $C_i = 2\zeta_i \omega_i M_i$ is the ith generalized damping, $K_i = \int_0^{L_B} E I \varphi_i''(x) \varphi_i''(x) dx$ is the ith generalized stiffness, $Q(t) = \int_0^{L_B} \varphi_i(x) [f(x,t) - \partial m(x,t)/\partial x] dx$ is the ith generalized force. Applying the initial condition m(x,t) = 0 and the tip force F(t), the generalized force can be written as $Q(t) = \varphi_i(L_B)F(t)$. Solving (16) using Duhamel's integral gives

$$y(x,t) = \sum_{i=1}^{+\infty} \frac{\varphi_i(x) \cdot \varphi_i(L_B)}{M_i \omega_{di}} \cdot \int_0^t F(\tau) \cdot e^{-\zeta_i \omega_i(t-\tau)} \cdot \sin \omega_{di}(t-\tau) d\tau.$$
 (16)

The relationship between displacement y(x, t) and strain ε is

$$\varepsilon = \mathbf{y}'' \cdot \mathbf{y}_0,$$
 (17)

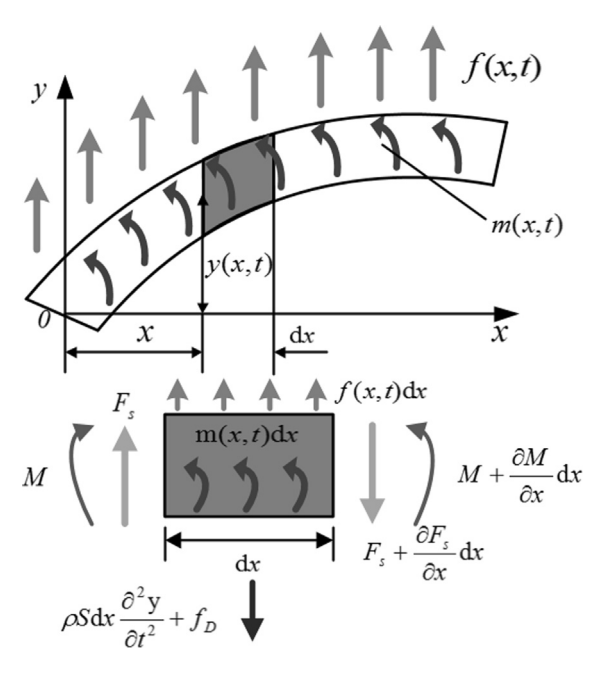


Fig. 4. Free body diagram of a differential beam element of the Fe-Ga beam. The external force is f(x, t), moment per unit length is m(x, t); Fs, M, and fD are the shear force, the moment on cross section, and the external damping force, respectively.

where y_0 is the distance from the neutral axis. Substituting (17) into (16) gives

$$\varepsilon(x,t) = \sum_{i=1}^{+\infty} \frac{\frac{\partial^2 \varphi_i(x)}{\partial x^2} \varphi_i(L_B)}{M_i \omega_{di}} \cdot \int_0^t F(\tau) \cdot e^{-\zeta_i \omega_i(t-\tau)} \cdot \sin \omega_{di}(t-\tau) d\tau \cdot y_0.$$
 (18)

When the moment of inertia *I* and area *S* are constants, the natural vibration frequency and mode shape of the beam are described by [36]

$$\cos\beta L_R \cdot \cosh\beta L_R + 1 = 0,\tag{19}$$

$$\varphi_i(x) = D_i[(\cos\beta_i x - \cosh\beta_i x) + \tau(\sin\beta_i x - \sinh\beta_i x)] = D_i \varphi_i(x), \tau = \frac{\sin\beta_i L_B - \sinh\beta_i L_B}{\cos\beta_i L_B + \cosh\beta_i L_B}, \tag{20}$$

where β_i is the *i*th solution for (19) and the coefficient D_i is

$$D_i = \sqrt{\frac{1}{\rho S} \frac{1}{\int_0^{L_B} \phi_i(x) \phi_i(x) dx}}.$$
 (21)

The relationship between β_i and ω_i is

$$\beta_i^4 = \rho S \omega_i^2 / EI. \tag{22}$$

Insertion of (22) into (19) gives

$$\omega_i = (\beta_i L_B)^2 \sqrt{\frac{EI}{\rho S L_B^4}}, \quad (i = 1, 2, 3 \cdots), \tag{23}$$

where

$$\beta_1 = \frac{1.875}{L_B}, \ \beta_2 = \frac{4.694}{L_B}, \ \beta_3 = \frac{7.855}{L_B}, \text{and} \ \beta_i \approx \frac{2i-1}{2L_B}\pi, \ (i \geq 3)$$

4.2. Analytical comparison between the rod and the rectangular beam

The performance of the rod and rectangular beam is compared in terms of average strain. A triangular impulse excitation force with an amplitude of 200 N and a rising time of 0.1 ms is applied to each configuration. The dimensions of the rod are $\phi = 100$ mm, and the dimensions of the rectangular beam are a = 100 mm, and the strain inside the Fe-Ga element is a direct indicator of the sensitivity according to (4). Hence, average strains a = 100 mm and a = 100 mm are the strain inside the Fe-Ga element is a direct indicator of the sensitivity according to (4). Hence, average strains a = 100 mm are the strain inside the Fe-Ga element is a direct indicator of the sensitivity according to (4).

$$\alpha_{R} = \frac{\int_{0}^{L_{R}} \epsilon(x) dx}{L_{R}}, \alpha_{B} = \frac{\int_{0}^{\frac{H}{2}} \int_{0}^{L_{B}} \epsilon(x, y_{0}) dx dy_{0}}{L_{R} \cdot \frac{H}{2}}, \tag{24}$$

where *H* is the thickness.

The first mode of each structure contributes the most to the impact response. Thus, average strains are evaluated using the first mode responses only. Fig. 5 shows the average strain with respect to time for the two configurations. The average strain of the beam is about 11.27 times higher than that of the rod. Thus, the beam configuration can reach a higher sensitivity.

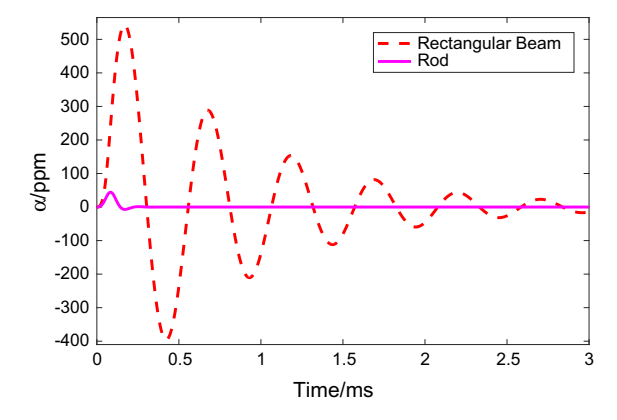


Fig. 5. Average strain for the rod and rectangular beam.

5. Optimal design for beam configuration

The sensitivity of the rectangular beam configuration can be further improved by changing the cross section. The I-section is widely used in engineering as it usually shows a better performance (higher stiffness and strength) than a trapezoidal section and T-section. This study therefore investigates the three cross section geometries as shown in Fig. 6, including a rectangular beam, a uniform I beam and a tapered I beam whose width decreases linearly along the length. The uniform I beam shares the same kinetic model with the rectangular beam, while the kinetic model for the tapered I beam can be obtained by employing the Rayleigh-Ritz method.

5.1. Kinetic model for tapered I beam

The geometry notations of the tapered I beam are defined in Fig. 7 which is shown as follows. The width W(x), cross section S(x), and moment of inertia I(x) for the tapered I beam shown in Fig. 7 are

$$W(x) = W_a + (W_b - W_a)x/L_B$$

$$S(x) = S_a[1 + (e - 1)x/L_B] ,$$

$$I(x) = I_a[1 + (e - 1)x/L_B]$$
(25)

where $I_a = W_a H^3 (1 - kr^3)/12$ is the moment of inertia in the fixed end, $S_a = W_a H (1 - kr)$ is the cross section in the fixed end, $e = W_b/W_a$, k = w(x)/W(x), and r = h/H.

The governing equation of the tapered I beam are the same as (14) and (18), while the vibration modes and natural frequencies are different. The ith mode is

$$\varphi_i(\mathbf{x}) = \sum_{i=1}^n a_{ij} \phi_{ij}(\mathbf{x}), \quad (j=1,2,3,\cdots,n),$$
(26)

where the basis function is $\phi_{ii}(x) = (1 - x/L_B)^{j-1}(x/L_B)^2$, and a_{ii} denotes the weights.

The homogeneous solution for the un-damped tapered I beam can be obtained by Rayleigh-Ritz method as

$$(\mathbf{K} - \omega_i^2 \mathbf{M}) a_{ij} = 0, \tag{27}$$

where $\mathbf{M} = [m_{ij}]$ and $\mathbf{K} = [k_{ij}]$ denote mass coefficient matrix and stiffness coefficient matrix. Here

$$m_{ij} = \int_0^{L_B} \rho S(x) \phi_i \phi_j dx = \rho S_a \int_0^{L_B} \left[1 + (e-1) \frac{x}{L_B} \right] \phi_i \phi_j dx,$$

$$k_{ij} = \int_0^{L_B} EI(x)\phi_i'' \cdot \phi_j'' dx = EI_a \int_0^{L_B} \left[1 + (e-1)\frac{x}{L_B} \right] \phi_i'' \phi_j'' dx.$$

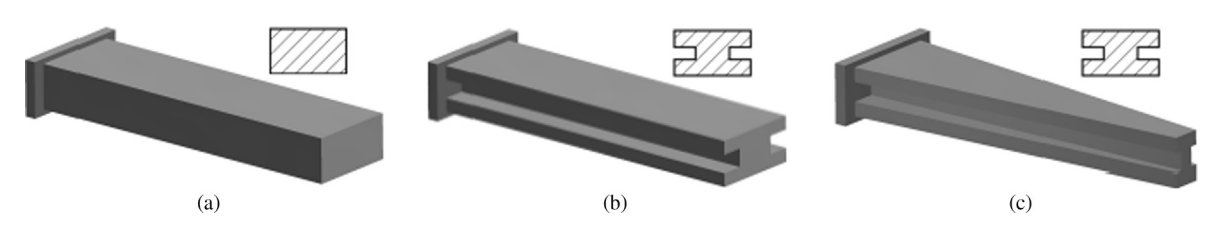


Fig. 6. (a) Rectangular beam, (b) uniform I beam, and (c) tapered I beam.

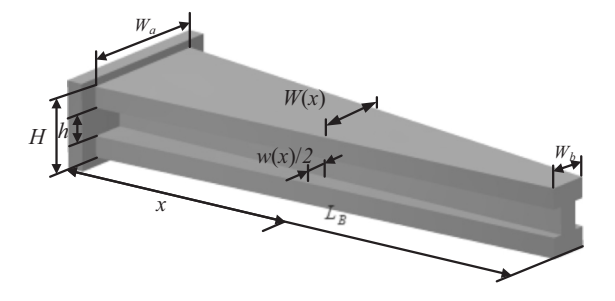


Fig. 7. Geometry of the tapered I beam.

To simplify the calculation, only the first five modes of the system are considered. Thus,

$$\mathbf{K} = \frac{EI_a}{105L_B^3} \, \mathbf{K}, \, \mathbf{\bar{K}} = \begin{bmatrix} 210(e+1) & -210e & 0 & 0 & 0 \\ -210e & 105(3e+1) & -42(e-1) & -21(e-1) & -12(e-1) \\ 0 & -42(e-1) & 42(e+1) & 6(2e+5) & 3(e+7) \\ 0 & -21(e-1) & 6(2e+5) & 9(e+3) & 5e+22 \\ 0 & -12(e-1) & 3(e+7) & 5e+22 & 4(e+5) \end{bmatrix}, \mathbf{M} = \rho S_a L_B \, \mathbf{\bar{M}},$$

$$\mathbf{\bar{M}} = \begin{bmatrix} \frac{5e+1}{30} & \frac{5e+2}{210} & \frac{5e+3}{840} & \frac{5e+4}{2520} & \frac{e+1}{1260} \\ \frac{5e+2}{210} & \frac{5e+3}{840} & \frac{5e+4}{2520} & \frac{1260}{13860} & \frac{5e+4}{27720} \\ \frac{5e+4}{840} & \frac{5e+4}{2520} & \frac{1260}{1260} & \frac{13860}{13860} & \frac{5e+7}{27720} \\ \frac{5e+4}{2520} & \frac{1260}{1260} & \frac{13860}{13860} & \frac{5e+7}{27720} & \frac{5e+8}{51480} & \frac{5e+9}{27920} & \frac{5e+8}{51480} & \frac{5e+9}{290090} \\ \frac{e+1}{1260} & \frac{5e+6}{13860} & \frac{5e+7}{27720} & \frac{5e+8}{514800} & \frac{5e+9}{90090} & \frac{5e+9}{514800} & \frac{5e+9}{90090} & \frac{5e+9}{514800} & \frac{5e+9}{90090} & \frac{5e+8}{514800} & \frac{5e+9}{90090} & \frac{5e+8}{514800} & \frac{5e+9}{90090} & \frac{5e+8}{514800} & \frac{5e+9}{90090} & \frac{5e+8}{514800} & \frac{5e+9}{90090} & \frac{5e+9}{514800} & \frac{5e+9}{90090} & \frac{5e+8}{514800} & \frac{5e+9}{90090} & \frac{5e+9}{514800} & \frac{5e+9}{900900} & \frac{5e+9}{514800} & \frac{5e+9}{90090} & \frac{5e+9}{514800} & \frac{5e+9}{900900} & \frac{5e+9}{9009000} & \frac{5e+9}{9009000} & \frac{5e+9}{9009000} & \frac{5e+9}{9009000$$

Rewriting the eigenvalue problem as $(\mathbf{K} - \lambda_i \mathbf{M}) a_{ij} = 0$, where $\lambda_i = (105 \rho S_a L_B^4)/(E I_a \omega_i^2)$, the natural frequency can be written as

$$\omega_i = \sqrt{\frac{\lambda_i}{105}} \cdot \sqrt{\frac{EI_a}{\rho S_a L_B^4}}.$$
 (29)

The values of a_{ij} and natural frequency ω_i can be obtained by substituting e, k, and r into (27), (28), and (29). Hence, the average strain can be obtained substituting natural frequencies and modes to (18) and calculating (24).

5.2. Orthogonal design for uniform and tapered I beam

An orthogonal design [37] is used to optimize the dimensions of the uniform and tapered I beam. As for the tapered I beam, e, k, and r are chosen as the design parameters. The main design objective is to maximize the sensitivity, which is represented by v_1 or the average strain normalized with respect to that of the rectangular beam. The stiffness and strength are additional design objectives, since a higher stiffness leads to a broader frequency bandwidth and a higher strength allows for a wider impact force range. The bending stiffness is characterized by v_2 , which is the ratio of the equivalent stiffness of the tapered I beam to that of the rectangular beam. The equivalent stiffness of a tapered I beam is calculated based on its potential energy. The deflection at any given x is $y(x) = Y_0[3x^2/(2L_B^2) - x^3/(2L_B^3)]$, where Y_0 is the free-end deflection. The equivalent potential energy is

$$V = \frac{1}{2} \int_0^{L_B} EI(x) \left[\frac{\partial^2 y(x)}{\partial x^2} \right]^2 dx = \frac{1}{2} \int_0^{L_B} EI_e \left[\frac{\partial^2 y(x)}{\partial x^2} \right]^2 dx, \tag{30}$$

where I_e is the equivalent moment of inertia of the tapered I beam. The equivalent stiffness is

$$EI_{e} = \frac{(e+3)(1-kr^{3})}{4}EI_{0}, \tag{31}$$

where $EI_0 = EB_aH^3/12$ denotes the bending stiffness of the rectangular beam, I_0 is the moment of inertia of the rectangular beam. The strength is characterized by v_3 , which is the ratio of I_a to I_0 . As a result, the criteria to evaluate the design results are selected as sensitivity v_1 , stiffness v_2 , and strength v_3 .

In this study, each design parameter varies from 0.3 to 0.7 in 0.1 steps. Thus, each design parameter has 5 levels. A comprehensive set of parameter combinations consists of 125 individual parameter groups. This study implements an orthogonal design method to reduce the number of parameter groups being simulated. The down selection of parameter groups is conducted following a pre-designed orthogonal table [37].

An orthogonal design table $L_{25}(5^6)$ [38] is selected corresponding to the level of the design parameters, where "25" denotes the total selected parameter groups, "5" denotes the level number for each selected design parameter, and "6"

Table 1 Level values for tapered I beam.

Level	е	k	r
0.7	2.1497	2.2654	2.2224
0.6	2.1892	2.2636	2.2394
0.5	2.2344	2.2513	2.2554
0.4	2.2942	2.2378	2.2641
0.3	2.3773	2.2268	2.2636

Table 2Level values for uniform I beam

Level	k	r
0.7	2.0850	2.0086
0.6	2.0787	2.0583
0.5	2.0762	2.0935
0.4	2.0768	2.1141
0.3	2.0798	2.1220

means the maximum design parameters that can be studied using this orthogonal table. The orthogonal design only calls the analytical model 25 times and is able to represent all the 125 parameter combinations.

The three criteria are analyzed simultaneously as $v = a_1 v_1 + a_2 v_2 + a_3 v_3$. The weights for each indicator are $a_1 = 0.5$, $a_2 = 0.8$, and $a_3 = 0.8$. They are chosen empirically according to the property and importance of the design objectives.

The indicator v of each selected group is first calculated. The values of v are then analyzed using the intuitive analysis method, in which the optimal design parameter is associated with the highest level value presented in Table 1. The level value is calculated by averaging v from certain parameter groups. For instance, the level value for e = 0.7 is the average of all the v values that are obtained from the selected parameter groups containing e = 0.7. According to Table 1, the level values of e, k, and r reach the maximum at level 0.3, 0.7, and 0.4, respectively. So the optimal design parameters are e = 0.3, k = 0.7, and r = 0.4.

As for the uniform I beam, the same method above is employed to optimize its dimensions, where k and r are chosen as the design parameters. The same orthogonal design table, design parameter levels, and design criterion v are used. The level values are shown in Table 2, which shows the optimal dimensions are k = 0.7 and r = 0.3.

6. Analytical comparison

The performance of the three beam configurations is compared in terms of average strain under a triangular impulse excitation force with an amplitude of 200 N and a rising time of 0.1 ms. The dimensions of each configuration are presented in Table 3, where (A) is the rectangular beam, (B) is the uniform I beam, (C) is the tapered I beam, and (D) is the uniform rod.

The first mode of each structure contributes the most to the impact response. Thus, average strains are evaluated using the first mode responses only. Fig. 8 shows the average strain with respect to time for each configuration. The frequency bandwidth of each impact sensor configuration is investigated by applying a sinusoidal force on the beam's tip. Fig. 9 shows the Bode plot of the strain versus excitation frequency.

Table 3 Size for three beams.

	L (mm)	B (mm)	H (mm)	e	k	r
A	30	8	4	=	-	_
В				_	0.7	0.3
C				0.3	0.7	0.4
D	$\phi 8 \text{ mm} \times 100 \text{ mm}$	n				

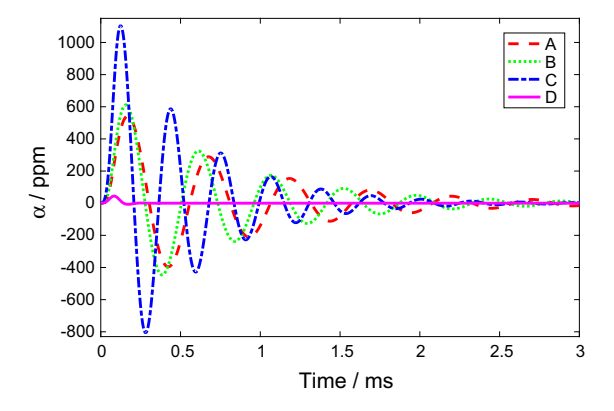


Fig. 8. Average strains of four configurations.

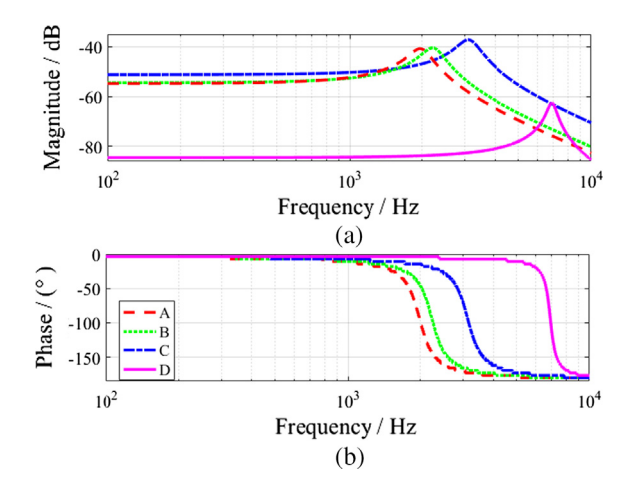


Fig. 9. Bode plot of the strain versus excitation frequency, (a) amplitude frequency plot and (b) phase frequency plot.

Table 4Average strain and frequency bandwidth comparison.

Configuration	Maximum Amplitude of Average Strain α (ppm)	Frequency Bandwidth (Hz)
Α	542.94	1982
В	611.78	2209
C	1105.50	3203
D	44.26	6903

It is seen from Fig. 8 that among the four configurations, the maximum average strain can be obtained based on the proposed tapered I beam design, which are 2.04, 1.81 and 24.97 times of design A, B, and D. The sensitivity of A and B are almost the same, and the rod configuration is the smallest.

The frequency responses of the four designs are illustrated in Fig. 9, which are compared to investigate the bandwidth of the different configurations. It is seen that the rod configuration has the largest bandwidth. However, the sensitivity is too small. This proves that the rod configuration is suitable for applications that require high bandwidth while sensitivity is not the major concern. In the three beam configurations, the proposed tapered I beam has the highest fundamental natural frequency.

Table 4 compares the specific values of the average strains and frequency bandwidths for the four designs. It is seen that the rod has the largest fundamental natural frequency but much smaller average strain or sensitivity. Among the three beam configurations, the best average strain and frequency bandwidth are achieved from the proposed tapered I beam. Hence, it is selected for further experimental analysis.

7. Experimental analysis

Impact force sensors based on the optimized Fe-Ga tapered I beam and the Fe-Ga rod are fabricated and tested. As shown in Fig. 10, the Fe-Ga rod based impact force sensor is equipped with a pair of electromagnets, which are driven by a constant current source. The field through the Fe-Ga rod is measured by a Hall-effect chip attached to the rod surface, where the Hall-effect chip is powered by a battery. The impact force is applied by an impact hammer (KSI-728A002). The output signal of the impact sensor is processed by a KSI-9201 signal conditioner. A 32-turn, 0.35 mm diameter, and 12 mm long pickup coil is placed around the Fe-Ga rod and converts stress-induced magnetization variation to a voltage signal. The corresponding flux density is obtained by integrating the voltage on the coil over time using a flux meter. All the experimental data are collected by an oscilloscope (TPS2024B). Fig. 11 shows a similar experimental setup for the tapered I beam. The beam has the same pickup coil as the rod. Compared to the rod, a single electromagnet is utilized to generate the bias magnetic field. The Hall-effect chip is placed close to the field end of the beam. Impact forces with similar amplitudes and rising time are applied on the tip of the beam using the same impact hammer.

7.1. Experimental comparison

The influence of the bias magnetic field is investigated experimentally by varying the DC current through the electromagnets from 0.08 A to 0.98 A. Impact forces with an amplitude of 50 ± 1 N are applied. Fig. 12 shows flux density B versus the corresponding impact force F.

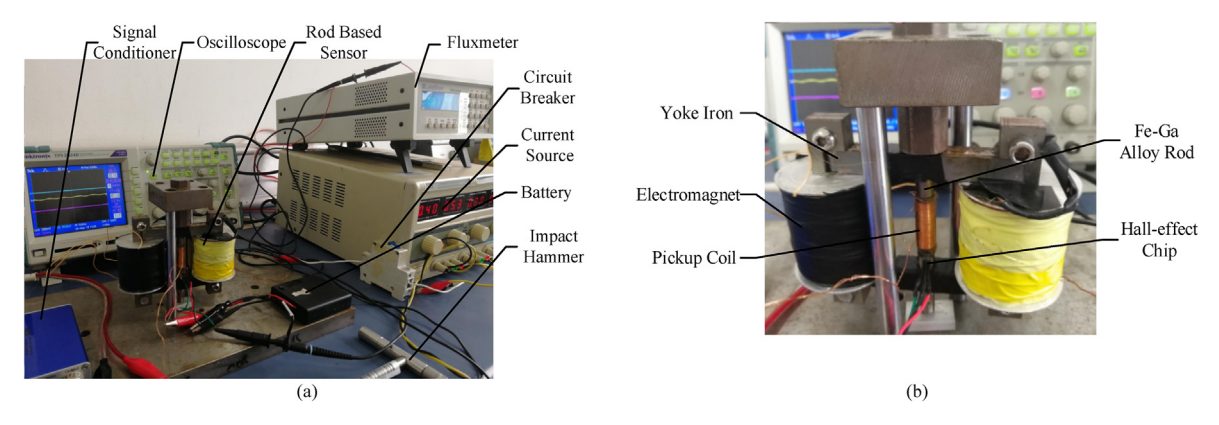


Fig. 10. (a) Data acquisition system and (b) zoom-in view of the Fe-Ga rod based impact force sensor. The two electromagnets are 1375-turn and 0.65 mm diameter; the pickup coil is 32-turn, 0.35 mm diameter, and 12 mm long.

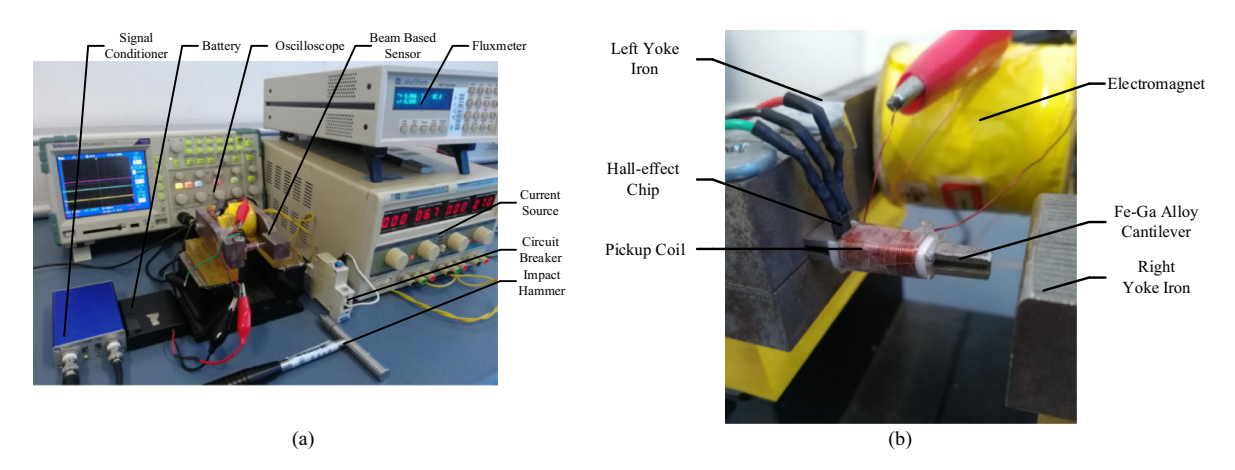


Fig. 11. (a) Data acquisition system and (b) zoom-in view of the Fe-Ga beam based impact force sensor. The electromagnet is 1497-turn and 0.5 mm diameter; the pickup coil is 32-turn, 0.35 mm diameter, and 12 mm long.

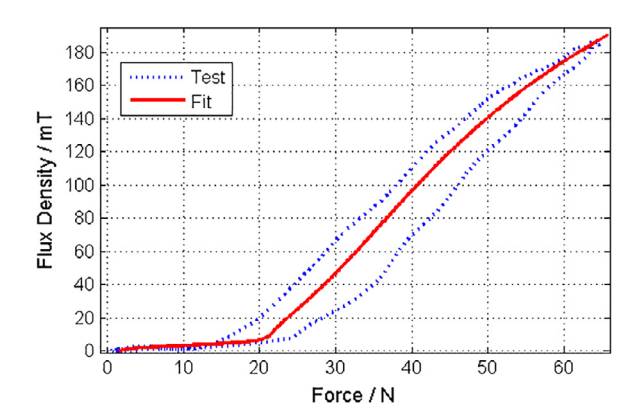


Fig. 12. Non-linear relationship between the force and the flux density. The blue test curve is obtained via experimental output of hammer and flux meter and the red fit curve is obtained via the Levenberg-Marquardt fitting method. (For interpretation of the references to color in this figure legend, the reader is referred to the web version of this article.)

The sensitivity, which is defined as B/F, is nonlinear. The sensitivity is relatively small when F is smaller than 20 N. This low sensitivity region can be avoided by applying a pre-compression to the cantilever beam. The measured flux density is $\mathbf{B} = [b_1, b_2, \dots, b_n]$ and the corresponding input impact force by impact hammer is $\mathbf{F} = [f_1, f_2, \dots, f_n]$. For comparison purposes, an average sensitivity is defined as

$$Sen_{ave} = \frac{1}{n} \sum_{i=1}^{n} Sen_i, \quad Sen_i = \frac{b_i}{f_i}, \tag{32}$$

Fig. 13 shows the sensitivity comparison between the rod and the tapered I beam. The experimental results confirm that the tapered I beam exhibits a sensitivity that is at least 13.5 times higher than that of the rod for all bias field conditions. Particularly, the sensitivity of the tapered I beam is about 27 times of that of the rod when the bias field is 14 kA/m, which is consistent with the analytical comparison (25 times).

The global magnetization of Fe-Ga alloys is the weighted sum of the magnetization of local magnetic domains. The orientation of each magnetic domain depends on the interplay of magnetic and mechanical inputs [39,40]. The magnetic domain tends to be aligned in parallel to the field direction while perpendicular to the compressive stress. For the beam configuration, the Fe-Ga alloy needs to be operated near the field-induced saturation to avoid the cancel-out effect, as discussed in Section 4. Fig. 14 shows the measured sensitivity values, where the bias magnetic field is near a saturation at 14 kA/m, and the bias magnetic field over 14 kA/m brings little benefit for sensitivity. In this study the optimal bias magnetic field is selected as 14 kA/m corresponding to a DC current of 0.58 A.

7.2. Force calibration

Under constant current biases, the nonlinear sensitivity is first introduced by the stress- and field-dependent piezomagnetic coefficient d [32]. This nonlinear sensitivity measured from experiments is fit following the Levenberg-Marquardt method [41].

The impact force measured by the impact hammer is $\mathbf{F} = \{f(b_i)\}, (i = 1, 2, \dots, n)$. The approximated force is $\mathbf{F}' = \{f'(b_i)\}$, where $f'(b_i)$ is an empirical function. So an n-dimensional residual vector for impact is

$$\mathbf{o}(\mathbf{p}) = \begin{bmatrix} f(b_1) - f'(b_1) \\ f(b_2) - f'(b_2) \\ \vdots \\ f(b_n) - f'(b_n) \end{bmatrix}, \tag{33}$$

where \mathbf{p} is the coefficient vector of the selected empirical function. The optimal parameter \mathbf{p} is

$$\mathbf{p} = \arg\min S(\mathbf{p}), S(\mathbf{p}) = \|\mathbf{o}(\mathbf{p})\|^2, \tag{34}$$

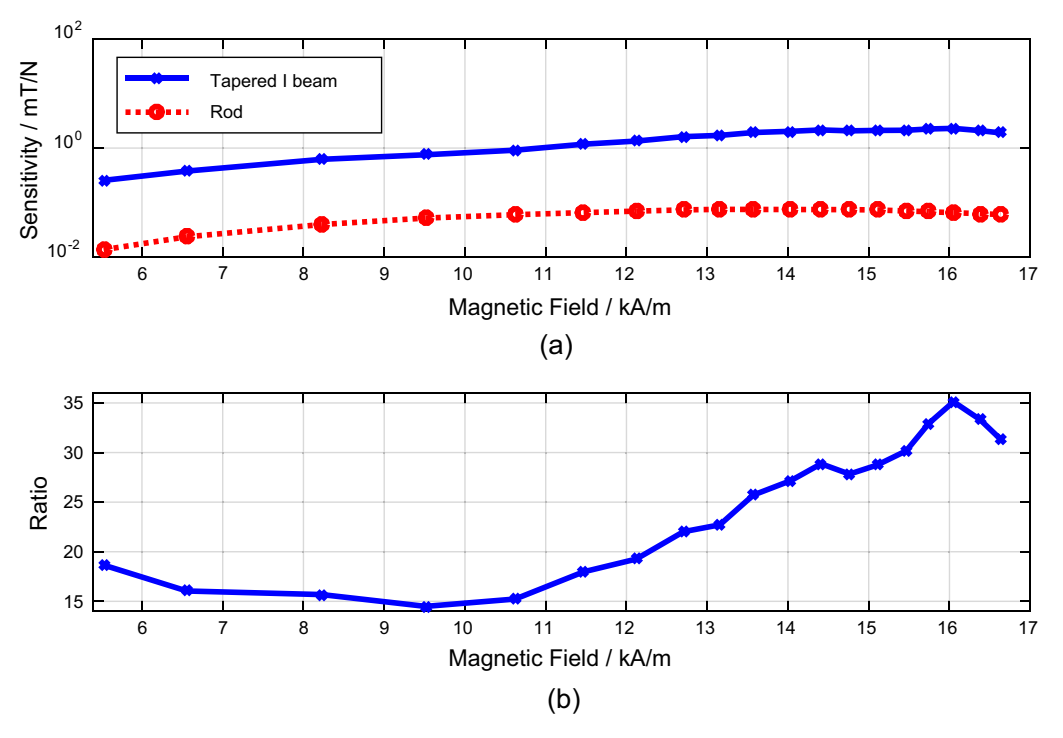


Fig. 13. (a) Sensitivity comparison between the rod and tapered I beam and (b) the sensitivity of tapered I beam to that of the rod.

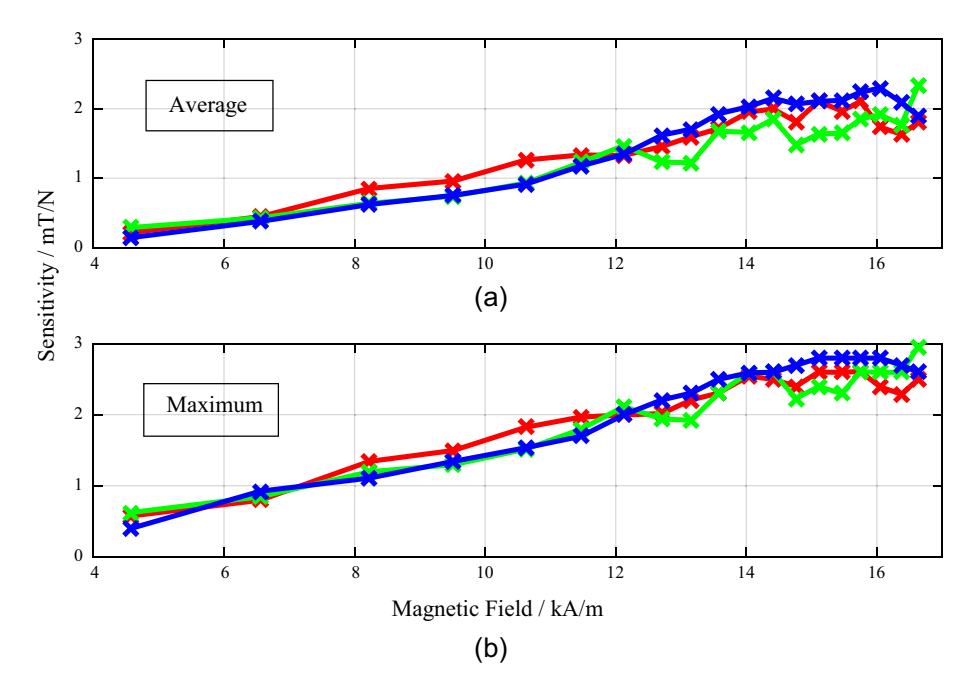


Fig. 14. Measured sensitivity versus bias magnetic field. Repeated experiments are developed to analyze the relationship between sensitivity and bias magnetic field; (a) average sensitivity and (b) maximum sensitivity.

where the Jacobi matrix $\nabla o(\mathbf{p})$ is

$$\nabla \mathbf{o}(\mathbf{p}) = \left[\nabla \mathbf{o}_1(\mathbf{p}), \nabla \mathbf{o}_2(\mathbf{p}), \cdots, \nabla \mathbf{o}_n(\mathbf{p})\right]^T. \tag{35}$$

The iterative formula of the Levenberg-Marquardt method is

$$\begin{aligned}
& \boldsymbol{p}_{k+1} = \boldsymbol{p}_k + \boldsymbol{z}_k \\
& \boldsymbol{z}_k = -\left[\nabla \boldsymbol{o}(\boldsymbol{p})^T \nabla \boldsymbol{o}(\boldsymbol{p}) + \gamma_k \boldsymbol{I} \right]^{-1} \cdot \nabla \boldsymbol{o}(\boldsymbol{p})^T \cdot \boldsymbol{o}(\boldsymbol{p}_k),
\end{aligned} \tag{36}$$

where \mathbf{z}_k is the iteration direction, the subscript k denotes the iteration number, and the damping factor γ is introduced into a Hessian matrix to avoid an ill-conditioned Hessian matrix.

The norm of the residual vector at kth step is calculated as

$$S(\boldsymbol{p}_k + \boldsymbol{z}_k)|_{\gamma_k} = \min_{\gamma > 0} S(\boldsymbol{p}_k + \boldsymbol{z}_k)|_{\gamma}. \tag{37}$$

The optimal approximate value is obtained when $\| \boldsymbol{o}(\boldsymbol{p}_{k+1}) - \boldsymbol{o}(\boldsymbol{p}_k) \|^2 < \Theta$, where Θ determines the convergence condition.

The selected fitting function is

$$f'(b) = \frac{\sum_{i=1}^{5} p_{2i-1} \cdot b^{i-1}}{1 + \sum_{i=1}^{5} p_{2i} \cdot b^{i}}.$$
 (38)

The coefficient set \mathbf{p} is calibrated using the data measured under an impact force amplitude of 64.7 N and the result is shown in Fig. 12.

$$\mathbf{p} = [1.563, 0.7020, 1.494, -0.2200, 0.2344, 0.04119, 0.3046, 0.001402, 0.05332, -4.091] \tag{39}$$

The same set of **p** is validated for other impact amplitudes (41.9 N, 51.5 N, and 61.7 N) as shown in Fig. 15. The measurement error is quantified by

Average Error =
$$\frac{1}{n} \sum_{i=1}^{n} \frac{\|f(b_i) - f'(b_i)\|}{f(b_i)}$$
. (40)

The Fe-Ga I beam, together with the Levenberg-Marquardt method, are able to accurately measure the impact force under varying amplitudes with an average error of 5.73%, 5.58%, and 3.85%, respectively. As shown in Fig. 12, Fe-Ga alloys exhibit hysteresis, but the experimental results show that the time delay due to material hysteresis is negligible and thus material hysteresis can be ignored in this sensor.

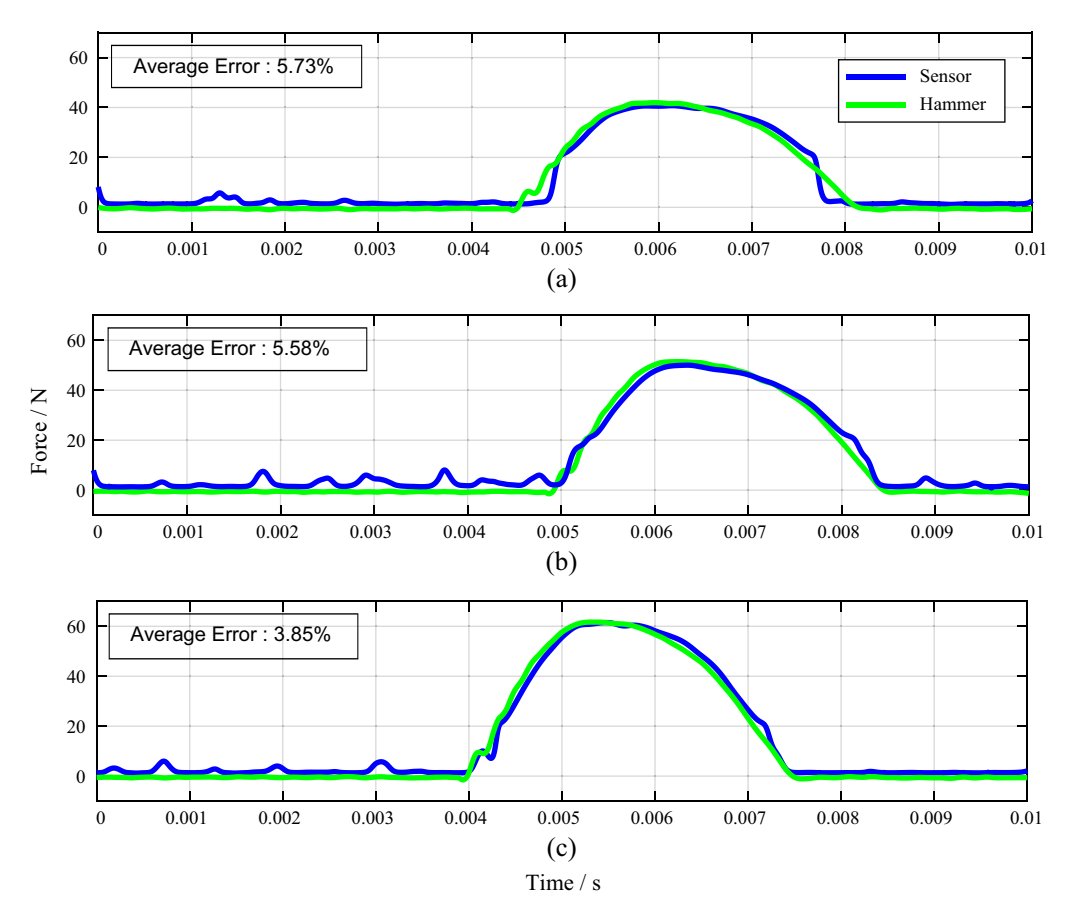


Fig. 15. Comparison of sensor measurement and impact hammer measurement for impact force amplitudes of (a) 41.9 N, (b) 51.5 N, and (c) 61.7 N, respectively.

8. Conclusion

This paper develops an impact force sensor, which consists of an electromagnet, magnetic circuit, Fe-Ga alloy, and pickup coil. The impact excitation is reflected by the resulting flux density measured from the pickup coil. The proposed tapered I beam is investigated analytically and numerically. A similar rod is modeled and tested for comparison purposes. Due to the relatively high axial stiffness, the rod generally provides a much smaller sensitivity and thus is not recommended for future applications. Three types of Fe-Ga beam geometries, including a rectangular beam, a uniform I beam, and a tapered I beam, are compared via analytical modeling. An orthogonal design method is implemented to optimize the beams' dimensions. The groove width, groove height, and beam width are optimized targeting the maximum sensitivity as well as frequency bandwidth and mechanical strength. The tapered I beam provides the maximum possible sensitivity. Compared to the rod, the sensitivity of the tapered I beam is 23.98 times higher than that of the rod according to analytical modeling results. Finally, the optimized tapered I beam sensor and the rod based sensor are fabricated and tested. Comparative measurements are conducted at varying bias fields. The experimental results confirm that the tapered I beam exhibits a sensitivity that is about 13.5 - 34.1 times higher than that of the rod for all bias field conditions. The optimal bias field is 14 kA/m for the beam configuration. The nonlinear relationship between measured flux density and input impact force is described by an empirical function whose coefficients have been obtained following the Levenberg-Marquardt method. The same set of parameters is validated for various impact force amplitudes. Experimental results shows that the measurement error from the proposed sensor is within 5.7% and the influence of the material hysteresis is negligible. Currently, the proposed sensors require electromagnets to generate a bias magnetic field. Future designs that utilize permanent magnets may be standalone and require no external power sources. The optimization in this study targets only the dimensions of the beam. Future work may develop fully-coupled system-level model and optimize for geometries and magnetic field systems simultaneously.

Acknowledgment

The authors would like to thank the National Natural Science Foundation of China under grant 51975418 and Wuhan University of Technology for their financial supports and Mr. Li P H, Mr. Chen D F and Mr. Zhao J W for their technical assistances. Support for Z.D. and M.J.D. comes from the member organizations of the Smart Vehicle Concepts Center (www. SmartvehicleCenter.org), a National Science Foundation Industry-University Cooperative Research Center established under grant IIP-1738723.

References

- [1] H. Wang, T. Nagayama, D. Su, Estimation of dynamic tire force by measurement of vehicle body responses with numerical and experimental validation, Mech. Syst. Signal Proc. 123 (2019) 369–385.
- [2] Y. Chuman, K. Mimura, K. Kaizu, S. Tanimura, A sensing block method for measuring impact force generated at a contact part, Int. J. Impact Eng. 19 (2) (1997) 165–174.
- [3] J. Zhang, Q. Xia, Y. Cheng, Z. Wu, Strain flexibility identification of bridges from long-gauge strain measurements, Mech. Syst. Sig. Process. 62 (2015) 272–283.
- [4] Y.H. Huang, L. Liu, F.C. Sham, Y.S. Chan, S.P. Ng, Optical strain gauge vs. traditional strain gauges for concrete elasticity modulus determination, Optik Int. J. Light Electron. Optics 121 (18) (2010) 1635–1641.
- [5] Z. Zhu, S. To, Y. Li, W. Zhu, L. Bian, External force estimation of a piezo-actuated compliant mechanism based on a fractional order hysteresis model, Mech. Syst. Signal Proc. 110 (2018) 296–306.
- [6] J. Fritz, K. Wünnemann, W.U. Reimold, C. Meyer, U. Hornemann, Shock experiments on quartz targets pre-cooled to 77 K, Int. J. Impact Eng. 38 (6) (2011) 440–445.
- [7] Z. Wang, H. Zhu, Y. Dong, G. Feng, Development of a High-Resolution Quartz Resonator Force and Weight Sensor With Increased Reliability, IEEE/ASME Trans. Mechatron. 9 (2) (2004) 399–406.
- [8] Y.J. Li, B.Y. Sun, J. Zhang, Z.Y. Jia, A novel parallel piezoelectric six-axis heavy force/torque sensor, Measurement 42 (5) (2009) 730-736.
- [9] A.L. Tonge, J. Kimberley, K.T. Ramesh, The mechanism of compressive unloading failure in single crystal quartz and other brittle solids, Int. J. Solids Struct. 49 (26) (2012) 3923–3934.
- [10] Y. Shapiro, G. Kosa, A. Wolf, Shape tracking of planar hyper-flexible beams via embedded PVDF deflection sensors, IEEE/ASME Trans. Mechatron. 19 (4) (2014) 1260–1267.
- [11] Y. Shapiro, A. Wolf, G. Kosa, Piezoelectric deflection sensor for a Bi-Bellows actuator, IEEE/ASME Trans. Mechatron. 18 (3) (2013) 1226-1230.
- [12] K. Kotian, L.M. Headings, M.J. Dapino, Stress averaging in PVDF sensors for in-plane sinusoidal and impact-induced stresses, IEEE Sens. J. 13 (11) (2013) 4444–4451.
- [13] S.K. Hwang, H.Y. Hwang, Study on signal characteristic analysis of multi-axis load measurement sensors, Smart Mater. Struct. 25 (11) (2016) 115004.
- [14] Y. Roh, V.V. Varadan, V.K. Varadan, Characterization of all the elastic, dielectric, and piezoelectric constants of uniaxially oriented poled PVDF films, IEEE Trans. Ultrason. Ferroelectr. Freq. Control 49 (6) (2002) 836–847.
- [15] A. Rezayat, V. Nassiri, B. De Pauw, J. Ertveldt, S. Vanlanduit, P. Guillaume, Identification of dynamic forces using group-sparsity in frequency domain, Mech. Syst. Signal Process. 70–71 (2016) 769–787.
- [16] R.J. Roesthuis, M. Kemp, J.J.V.D. Dobbelsteen, S. Misra, Three-dimensional needle shape reconstruction using an array of fiber bragg grating sensors, IEEE/ASME Trans. Mechatron. 19 (4) (2014) 1115–1126.
- [17] J. Gomez, I. Jorge, G. Durana, J. Arrue, J. Zubia, Proof of concept of impact detection in composites using fiber Bragg grating arrays, Sensors 13 (9) (2013) 11998–12011.
- [18] K. Oman et al, Instrumentation of integrally stiffened composite panel with fiber Bragg grating sensors for vibration measurements, Smart Mater. Struct. 24 (8) (2015) 085031.
- [19] N. Adelsberg, Y. Weber, A. Yoffe, D. Shilo, Wireless thin layer force sensor based on a magnetostrictive composite material, Smart Mater. Struct. 26 (6) (2017) 065013.
- [20] W.J. Kim, A. Sadighi, A novel low-power linear magnetostrictive actuator with local three-phase excitation, IEEE/ASME Trans. Mechatron. 15 (2) (2010) 299–307.
- [21] H.M. Zhou, M.H. Li, X.H. Li, D.G. Zhang, An analytical and explicit multi-field coupled nonlinear constitutive model for Terfenol-D giant magnetostrictive material, Smart Mater. Struct. 25 (8) (2016) 085036.
- [22] A.E. Clark, J.B. Restorff, M. Wun-Fogle, T.A. Lograsso, Magnetostrictive properties of body-centered cubic Fe-Ga and Fe-Ga-Al alloys, IEEE Trans. Magn. 36 (5) (2000) 3238–3240.
- [23] Z.X. Deng, M.J. Dapino, Magnetic flux biasing of magnetostrictive sensors, Smart Mater. Struct. 26 (5) (2017) 055027.
- [24] T. Fett, D. Munz, G. Thun, Tensile and bending strength of piezoelectric ceramics, J. Mater. Sci. Lett. 18 (23) (1999) 1899–1902.
- [25] B.P. Baillargeon, S.S. Vel, Active vibration suppression of sandwich beams using piezoelectric shear actuators: Experiments and numerical simulations, J. Intell. Mater. Syst. Struct. 16 (6) (2005) 517–530.
- [26] B. Li, P.H. Li, L. Shu, D.F. Chen, Parametric design and experimental research for an iron-gallium alloy force sensor, Sensors and Materials 28 (3) (2016) 261–270.
- [27] G.D. Liu, Z.H. Dai, Z.H. Liu, J.L. Chen, G.H. Wu, Structure, magnetostriction, and magnetic properties of melt-spun Fe-Ga alloys, J. Appl. Phys. 99 (9) (2006), ID: 093904.
- [28] B.A. Cook, J.L. Harringa, T. Hansen, Electrical and thermal properties of Tb_{0.3}Dy_{0.7}Fe_{2-x}, J. Appl. Phys. 87 (2) (2000) 776–780.
- [29] M.J. Dapino, Z. Deng, F.T. Calkins, A.B. Flatau, Magnetostrictive Devices, Wiley Encyclopedia of Electrical and Electronics Engineering, John Wiley & Sons, Inc, New York, NY, USA, 2016.
- [30] J.J. Scheidler, V.M. Asnani, M.J. Dapino, Frequency-dependent, dynamic sensing properties of polycrystalline galfenol (fe81.6ga18.4), J. Appl. Phys. 119 (24) (2016), pp. 043001–220.
- [31] Z. Deng, M.J. Dapino, Review of magnetostrictive vibration energy harvesters, Smart Mater. Struct. 26 (10) (2017) 103001.
- [32] L. Weng, T. Walker, Z. Deng, M.J. Dapino, Major and minor stress-magnetization loops in textured polycrystalline Fe81.6Ga18.4 Galfenol, J. Appl. Phys. 113 (2) (2013), pp. 043001–595.
- [33] W.T. Thomson, M.D. Dahleh, Theory of Vibration with Applications, Tsinghua University Press, Beijing, China, 2005, pp. 271–276.
- [34] T. Ueno, S. Yamada, Performance of energy harvester using iron-gallium alloy in free vibration, IEEE Trans. Magn. 47 (10) (2011) 2407–2409.
- [35] S. Kita, T. Ueno, S. Yamada, Improvement of force factor of magnetostrictive vibration power generator for high efficiency, J. Appl. Phys. 117 (17) (2015) 3238–3240.
- [36] A. Simpson, Transverse modes and frequencies of beams translating between fixed end supports, J. Mech. Eng. Sci. 15 (3) (1973) 159-164.
- [37] H.J. Wang et al, Optimization of ultrasonic-assisted extraction of cordycepin from Cordyceps militaris using orthogonal experimental design, Molecules 19 (12) (2014) 20808–20820.
- [38] P. Duan, Y. Wang, Y. Yang, L. Dai, Optimization of adiponitrile hydrolysis in subcritical water using an orthogonal array design, J. Solution Chem. 38 (2) (2009) 241–258.

- [39] L. Shu, L. Headings, M.J. Dapino, D. Chen, Q. Lu, Nonlinear model for Galfenol cantilevered unimorphs considering full magnetoelastic coupling, J. Intell.
- Mater. Syst. Struct. 25 (2) (2014) 187–203.

 [40] L. Shu, M.J. Dapino, G. Wu, D. Chen, Frequency-dependent sliding-mode control of Galfenol-driven unimorph actuator based on finite-element model, IEEE Trans. Ind. Electron. 63 (2) (2016) 1071–1082.
- [41] J. Fan, J. Pan, A note on the Levenberg-Marquardt parameter, Appl. Math. Comput. 207 (2) (2009) 351-359.